Neotethys seawater chemistry and temperature at the dawn of the end Permian mass extinction

Claudio Garbelli[a*], Lucia Angiolini[a], Uwe Brand[b], Shuzhong Shen[c], Flavio Jadoul[a], Renato Posenato[d], Karem Azmy[e], Changqun Cao[c]

[a]Dipartimento di Scienze della Terra, Via Mangiagalli 34, Università di Milano, 20133 Milan Italy

[b]Department of Earth Sciences, Brock University, St. Catharines, Ontario L2S 3A1 Canada

[c]State Key Laboratory of Paleobiology and Stratigraphy, Nanjing Institute of Geology and Palaeontology, Chinese Academy of Sciences, Nanjing, Jiangsu 210008, P.R. China

[d]Dipartimento di Fisica e Scienze della Terra, Università di Ferrara, Polo Scientifico-tecnologico, Via Saragat 1, 44121 Ferrara Italy

[e]Department of Earth Sciences, Memorial University, St. John's, NL A1B 3X5 Canada

Contact author: C. Garbelli*

ABSTRACT

The end of the Permian was a time of great death and massive upheaval in the biosphere, atmosphere and hydrosphere. Over the last decades, many causes have been suggested to be responsible for that catastrophe such as global warming, anoxia and acidification. The Gyanyima limestone block was an open ocean seamount in the southern Neotethys at subtropical latitude, and it affords us insight into open-ocean oceanographic changes during the end of the Permian After careful screening using multiple tests, we reconstructed carbonate/seawater curves from the geochemical data stored in pristine brachiopod shell archives from the shallow water limestone of the Changhsingian Gyanyima Formation of Tibet. The reconstructed strontium isotope curve and data for the late Changhsingian is relatively invariant about 0.707013, but in the upper part of the succession the values become more radiogenic climaxing at about 0.707244. The $^{87}Sr/^{86}Sr$ curve and trend is similar to that observed for the Upper Permian succession in northern Italy, but dissimilar (less radiogenic) to whole rock results from Austria, Iran, China and Spitsbergen. The Ce/Ce* anomaly results. ranging from 0.310 to 0.577 for the brachiopods and from 0.237 to 0.655 for the coeval whole rock before the event, and of 0.276 for whole rock during the extinction event, suggest normal redox conditions. These Ce* values are typical of normal open-ocean oxic water quality conditions observed in modern and other ancient counterparts. The biota and Ce* information clearly discounts global anoxia as a primary cause for the end-Permian biotic crisis. Carbon isotopes from brachiopod shells and whole rock are relatively invariant for most of the latest Permian interval, which is in stark contrast to the distinct negative carbon isotope excursion observed near and about the event. Estimates of seawater temperature at shallow depth fluctuated from 22.2 to 29.0 °C up to unit 8-2, and then gradually rise from 29.7 °C in unit 8-13 to values exceeding 35 °C at a stratigraphic level about 120 ky before the Permian-

Triassic boundary, and just before the onset of the extinction interval. This dramatic increase in seawater temperature has been observed in global successions from tropical to mid latitude and from restricted to open ocean localities (e.g., northern Italy, Iran). The brachiopod archive and its geochemical proxies from Tibet support the paradigm that global warming must have been an important factor of the biotic crisis for the terrestrial and marine faunas and floras of the late Paleozoic world.

Keywords: brachiopods; carbon, oxygen and strontium isotopes; REE; seawater redox and temperature; Neotethys seawater

1. Introduction

The Permian was the theatre of major global changes in the Earth's geodynamics, climate, and seawater/atmosphere geochemistry. In that changing world, the biotic response to flood basalt volcanism, high pCO_2 and associated rapid warming was dramatic (Retallack, 2013; Burgess et al., 2014). Facilitated by anoxia (Isozaki, 1997; table 2, Brand et al., 2012a) and/or ocean acidification (Clarkson et al., 2015), it culminated in the end Permian mass extinction (e.g., Erwin, 2006; Shen et al., 2011; Brand et al., 2012a).

Notwithstanding the plethora of studies focusing on the end Permian-Early Triassic time interval and trying to determine the causes of the extinction, so far no single cause has been identified as the leading one. However, global warming is considered by some authors as the leading cause for the biotic crisis at the end of the Permian (Kearsey et al., 2009; Brand et al., 2012a; Chen et al., 2013; Retallack, 2013; Burgess et al., 2014).

Here, we provide new information on the end Permian mass extinction from a different perspective, focusing on a biogenic archive covering the pre-extinction interval,

78 and coming from a subtropical and open-ocean setting, which may be compared to the
79 present-day Bermuda. In this perspective, after extensive screening, the biogenic archive
80 was chosen to extract paleoenvironment information of fundamental importance in
81 obtaining a pristine geochemical signal of the end Permian Neotethys seawater. This is
82 why we selected brachiopods from among the inhabitants of Paleozoic shallow-water
83 benthic communities, because they were sensitive to global changes in the oceans during
84 this extreme event. Also, their potential for storing pristine archival information is high,
85 since they precipitate a low-Mg calcite shell that resists diagenesis and are found to be low
86 metabolic and physiologically unbuffered organisms (Payne and Clapham, 2012).
87 Furthermore, brachiopods are also known to precipitate their shell (secondary-tertiary
88 layers) in isotopic equilibrium with ambient seawater (e.g., Lowenstam, 1961; Carpenter
89 and Lohmann; 1995; Parkinson et al., 2005; Brand et al., 2003, 2011, 2013). Thus, they
90 are deemed one of the best carriers of primary proxies (trace elements, $\delta^{13}C$, $\delta^{18}O$,
91 $^{87}Sr/^{86}Sr$, ΣREE and Ce*) able to unravel the seawater/atmosphere geochemistry and
92 temperature during the Late Permian (e.g., Veizer et al, 1999; Brand et al., 2003; Korte et
93 al., 2005; Zaky et al., 2015).
94 A limitation of the brachiopod archive is its discontinuous record due to the Signor-
95 Lipps effect (Signor and Lipps, 1982) and to lithofacies change, thus resulting in an
96 absence or scarcity of specimens in some sediments of the uppermost Permian
97 succession (e.g., Angiolini et al., 2010). To overcome this difficulty, we selected the
98 Gyanyima section in southwestern Tibet (Wang et al., 2010; Shen et al., 2010), which is
99 characterized by high and continuous sedimentation during the latest Permian and by
100 biostratigraphically constrained and well-preserved brachiopods up to a few meters below
101 the Permian-Triassic boundary.
102 This leads us to the second focus of our research: the lastest Permian interval or
103 what we call the dawn of the extinction, which may have lasted hundreds to tens of

104 thousands of years (Shen et al., 2011; Brand et al., 2012a; Burgess et al., 2014), to infer
105 what seawater conditions were like immediately prior to the extinction and the implications
106 about the causal mechanism(s) and the timing of the extinctions itself. In particular, among
107 the parameters that may have changed dramatically, we are mostly interested to
108 investigate the temperature rise and the oxygenation state of seawater leading up to this
109 most important event. Finally, the third focus concerns the settings of end Permian
110 sequences. Many studies have described the end Permian crisis in equatorial settings
111 such as South China, Iran and northern Italy (e.g., Shen et al., 2011; Brand et al., 2012a;
112 Schobben et al., 2014 and references therein), but few describe in any detail what
113 happened at higher latitudes (Shen et al., 2006).
114 The aim of our study is to investigate the geochemistry (trace elements, $\delta^{13}C$, $\delta^{18}O$,
115 $^{87}Sr/^{86}Sr$, ΣREE and Ce*) of brachiopod shells from the Gyanyma section located at
116 subtropical latitude in the southern Neotethys, to 1) interpret their biochemical response
117 before and at the onset of the latest Permian event, 2) evaluate and constrain in time the
118 temperature rise and seawater redox, and 3) garner a better understanding of how
119 Neotethys seawater and/or Late Permian atmosphere may have changed before and
120 during the Earth's greatest biotic crisis.
121
122 2. **Geological setting**
123 The Gyanyima section (30°43'13.5''N and 80°41'42.4''E) was studied by a number
124 of authors (Wang and Xu, 1988; Guo et al.,1991; Shen et al., 2001, 2003; Crasquin-
125 Soleau et al., 2007; Shen et al., 2010; Wang et al. 2010). It is located in Burang County,
126 Ngari Region in southwestern Tibet, China, and is about 50 km northwest of the Town of
127 Burang (Fig. 1). The section consists of 350 m of Lopingian-Lower Triassic reefal and
128 bioclastic limestones, which outcrops 30–50 km south of the Indus-Tsangbo (=Yarlung-
129 Zangbo) Suture Zone that separates the Lhasa Block from the Himalaya Tethys Zone to

130 the south. Based on its reefal carbonates and interbedded thick basalts, the large block
131 that contains the Gyanyima section has been interpreted as a carbonate platform on a
132 Neotethyan seamount (Shen et al., 2001, 2003, 2010).
133 The investigated section (Fig. 2) comprises the Lopingian Gyanyima Formation that
134 is rich in foraminifers, corals, brachiopods and ostracods, and the overlying Triassic
135 Lanchengquxia Formation. The Gyanyima Formation is subdivided into 10 units for a total
136 thickness of about 310 meters (Fig. 2); units 1, 6, 9 and 10 are dominated by reefal
137 limestone (bafflestone and framestone) with rare bioclastic limestone (packstone and
138 grainstone). Unit 2 contains micritic limestone; units 3 and 4 consist of bioclastic limestone;
139 unit 5 consists of submarine basalt; unit 7 comprises micritic limestone, with shale and
140 reefal limestone; unit 8 and part of unit 9 contain cherty limestone. In particular, the
141 limestone from unit 9 (sample T-9-33) to the base of the overlying Lanchengquxia
142 Formation (unit 11; Y-11-1) consists of bioclastic packstones and grainstones with
143 brachiopods, gastropods, echinoderms, bryozoans, foraminifers, green algae, and
144 *Tubiphytes*, and alternating boundstone dominated by corals and sponges. These
145 biofacies suggest infralittoral shallow to open subtidal environments around fair-weather
146 wave base, and well oxygenated and normal salinity seawater during deposition of the
147 Gyanyima sediments (see supplementary figure 2). The Triassic samples from unit 11 (Y-
148 11-2 to Y-11-4) consist of fine-grained grainstone with crinoids, bivalves, ostracods,
149 calcispheres, and widespread Fe-oxide covering the bioclasts, the matrix, and the
150 syntaxial cements and locally concentrated along hardground/firmground thin horizons.
151 These observations and the biogenic allochems record a deepening trend below fair-
152 weather wave base, a crisis in the carbonate factory and lower sedimentation rates at the
153 Permian-Triassic boundary in the Tibetan seamount. All samples from units 9 to 11
154 (sample 11-4) show the same marine early diagenetic paragenesis with non-luminescent
155 scalenohedral to equant calcite cement. Above level Y-11-34, the sediments are

pervasively dolomitized (equidimensional mosaics of zoned, Fe-rich dolomitic crystals), with microbialites. In fact, Shen et al. (2010, p. 4) reported thrombolites and stromatolite-like structures that possibly suggest restricted peritidal environments. However, due to the pervasive dolomitization, it is difficult to evaluate the original depositional depth of unit 11.

Except for the first meter of unit 11, we confirm that the overall succession was deposited in a normal marine, subtidal environment as suggested by Shen et al. (2010) and Wang et al. (2010). Wang et al. (2010) described a rich foraminiferal fauna from the Gyanyima Formation and subdivided it into two biozones: (1) a lower *Colaniella parva* Biozone, and (2) an upper *Colaniella parva- Dilatofusulina orthogonios –Urushtenella* Biozone. The upper biozone is late Changhsingian (Wang et al., 2010), and consequently that infers a lower Changhsingian age for the lower biozone. In fact, a recent discussion (Vachard, 2014) on the distribution of *C. parva* underscores the fact that it has not been found in rocks older than late Changhsingian. This suggests that the sediments of the Gyanyima Formation may be limited to the upper Changhsingian, as *C. parva* occurs in its basal unit. However, in the absence of other biostratigraphic data, we prefer to maintain a conservative approach, and follow Wang et al. (2010) who considered the 310 m sequence belonging to the Changhsingian.

Conodonts are rare in the Permian part of the Tibetan succession possibly due to the reefal environment (Shen et al., 2010), but they become abundant in the Triassic Lanchengquxia Formation. More specifically, the abundance of the Griesbachian (Induan) conodonts *Clarkina carinata* and *C. tulongensis* 1.3 m above the base of the Lanchengquxia Formation allows us to tentatively constrain the Permian-Triassic boundary at the Gyanyima section between horizons Y-11-1 and Y-11-2 (Shen et al., 2010, fig. 6; Appendix 3).

3. Materials

Rhynchonelliformea brachiopods and host limestone samples were collected from a number of horizons (Appendix 1B and 2) of the Gyanyima section (30°43′13.5″N, 80°41′46.4″E) located in Burang County in the Ngari Region of southwestern Tibet, China (Shen et al., 2010). Nineteen species were investigated: the Productida *Costiferina spiralis* (Waagen 1884), *Costiferina subcostata* (Waagen, 1884), *Costiferina indica* (Waagen, 1884), *Richthofenia lawrenciana* (de Koninck, 1863), *Marginalosia* sp. ind., and *Costatumulus* sp. ind.; the Orthida *Enteletes* sp. ind. and *Acosarina minuta* (Abich, 1878); the Rhynchonellida *Stenoscisma gigantea* (Diener, 1897) and *Stenoscisma* sp.; the Athyridida *Araxathyris* sp. ind.; the Spiriferida *Neospirifer* sp. ind., *Martinia* sp. ind., *Permophricodothyris* sp. ind., and *Alphaneospirifer* sp; the Terebratulida *Hemiptychina* sp. ind., *Notothyris* sp. ind., and *Dielasma* sp. ind. Their biostratigraphic frameworks have been studied in detail by Shen et al. (2010) and Wang et al. (2010) and the reader is referred to these articles for further information.

4. Methods

Multiple screening tests were applied in order to evaluate the state of preservation of the shells (e.g., Brand et al., 2011; Ullman and Korte, 2015). Brachiopod shells were examined under scanning electron microscope (SEM), cathodoluminescence (CL) and polarizing microscope to evaluate the degree of preservation of shells.

For the microstructural investigation by SEM, specimens were cut along their longitudinal axis, embedded in resin, polished and then etched with 5% HCl for 15 s, gold-coated, and then scanned by SEM. SEM analyses were performed at NIGPAS using a LEO 1450 VP SEM and at the Department of Earth Sciences “A. Desio” with a Cambridge S-360 SEM.

Specimens were thin sectioned and uncovered thin sections were analyzed for luminescence evidence with a Nuclide ELM2 cold-cathode luminoscope operating at 10 kV

with a beam current of 5–7 mA. Electron beam exposure (before taking the photo) was limited to 15–30 s, so not to damage shell material due to excessive electron bombardment. Photographic exposure time was set to range from 1 to 4 seconds with a Nikon Coolpix 4500 operating at 200 ISO.

Samples for geochemical analyses were microdrilled from the cleaned mirror-image slab, under binocular microscope, from the central non-specialized innermost region (inner secondary layer and tertiary layer) of the ventral valve, or as specified in Appendix 3. We avoided sampling dorsal valves and specialized regions such as dental plates, the cardinal process, muscle scars, as well as the primary layer and the external part of the secondary layer, following the suggestions of Carpenter and Lohmann (1995), Parkinson et al. (2005) and Cusack et al. (2012). In selected specimens, we sampled specialized regions in order to evaluate the presence of a vital effect or kinetic fractionation related to different growth rates (Brand et al., 2013; Yamamoto et al., 2013).

A subset of brachiopods (42) and enclosing whole rock (38) was analyzed for trace elements and stable isotopes. About 20 mg of powder, weighed accurately of each sample was digested with 10 mL of purified 2 % (v/v) HNO_3. Chemical modifiers (K and La solutions) were added to all solutions, where appropriate (Ca and Sr tests), to counter chemical interference. High-purity reference standards (Delta Scientific) were used for calibration of the atomic absorption spectrophotometer (AAS) for each element. All samples were analyzed on a VARIAN 400P AAS for Ca, Mg, Sr, Mn and Fe at Brock University. Long-term precision and accuracy, based on the mean of 84 analyses of standard reference material (SRM) NBS 633 was 5.28, 1.44 (Ca), 6.29, 1.12 (Mg), 8.61, 0.69 (Sr), 5.36, 2.16 (Mn) and 11.12, 3.21 (Fe) relative percent (±%), respectively, of certified SRM values.

The brachiopod and whole-rock samples from Tibet were analyzed for carbon and oxygen isotopes at Memorial University. About 200 µg of powder of each sample was

reacted with ultrapure 100 % orthophosphatic acid at 50°C in a Thermo-Finnigan Gasbench II, and liberated CO_2 gas was introduced into a Thermo-Finnigan Delta V mass spectrometer. Long-term precision and accuracy compared to NBS-19 standard values were better than 0.05 ‰ for both $\delta^{13}C$ (+1.95 ‰) and $\delta^{18}O$ (-2.20 ‰) certified values.

Strontium isotope analyses were performed on a subset of brachiopods at Ruhr University, Bochum. About 1 mg of each sample was digested with 2.5 N suprapure HCl for about 24 h at room temperature. This was followed by chromatographic separation with 2.5 mL of AGW 50 x 8 (Biorad) cation exchange resin to obtain purified Sr. Samples were prepared and analyzed on a Finnigan MAT 262 7-collector solid-source mass spectrometer with single Re filament applying 1 µL of ionization enhancing solution (Birck, 1986). Loading blank was < 5 pg, column blank was < 1 ng, and reagent blank was < 0.01 ppb. The mean of 279 analyses of NIST standard NBS 987 was 0.710242 with a mean standard error of 0.000002 (±2 se) and mean standard deviation of 0.000032 (±2 sd), whereas the mean of 253 analyses of the USGS EN-1 standard was 0.709162 with a mean standard error of 0.000002 (±2 se) and mean standard deviation of 0.000026 (±2 sd). The strontium isotope values of this study were bracketed by and corrected to a nominal NBS-987 value of 0.710247 (McArthur et al., 2001).

Rare Earth element (REE) analyses were performed on some brachiopods and their enclosing rocks at Memorial University following the protocol described in Azmy et al. (2011, 2012) and Zaky et al. (2015). About 5 mg of powder of each sample was digested in 0.2 M HNO_3 for 70-80 min, analyzed by standard addition method using a Perkin Elmer Sciex Elan DRCII ICP-MS. Relative uncertainty (accuracy and precision) compared to SRM DLS 88a certified values are better than ±5 % (Azmy et al., 2011). The weak acid leach used in this method only captures soluble elements associated with the soluble carbonate fraction and leaves the non-carbonate materials essentially untouched and a non-contributory factor to the reported trace and REE chemistry of the samples from Tibet.

For REE results, shale-normalized Ce/Ce^*_{SN} (Ce^*) values of > 1 represent anoxic depositional conditions, whereas < 1 represent oxic ones (e.g., de Baar et al., 1988; Bau and Dulski, 1996; Azmy et al., 2011; Zaky et al., 2015). All geochemical results are found in Appendix 3.

5. Results

5.1. End Permian extinction at Gyanyima, Tibet

The faunal pattern of the latest Permian extinction in the Gyanyima section has been discussed by Shen et al. (2010) who showed it to be abrupt, similar to that observed in several other peri-Gondwanan and Tethyan successions (Angiolini et al., 2010; more references therein). However, based on the taxa distribution shown in Shen et al. (2010, fig. 2), we recalculated the position of the extinction boundary with the method of Wang and Marshall (2004), the pattern of extinction following Meldahl (1990), and the duration of the extinction according to the procedure by Wang et al. (2012); see Appendix 1A/B for details of the calculations. In doing this, we assumed uniform preservation as the facies is rather uniform up to the base of unit 11 (horizon Y-11-1). The results are plotted in Fig. 2 and show, (1) the upper envelope of the extinction represented by the extinction boundary at the 96% confidence interval at which all taxa go extinct, (2) the hollow curve of taxa distribution which matches the pattern of a sudden extinction as simulated by Meldahl (1990), and (3) the stratigraphic interval of the maximum duration of the extinction. With a confidence interval of 95% the event took place over the topmost 9 m of the Gyanyima Formation. Assuming a constant sedimentation rate for deposition of the bioclastic and reefal limestones of unit 1 to base of unit 11 and a duration of about 2.238 My for the Changhsingian (Shen et al., 2011, 2013; Burgess et al., 2014), this is equivalent to a time frame of one million years per 121 m of sediment, excluding deposition of the basalts (unit 5). Thus, the duration of the extinction event (at the 95% CI) corresponds to about 74 ky, to which we have to add the time for the deposition of 19 cm of condensed limestone

between horizon Y-11-1 and Y-11-2. This has been evaluated to correspond to 14 ky based on the depositional rate of condensed limestone and shale in North Iran (Schobben et al., 2014, Ghaderi et al., 2014). In conclusion, the maximum duration of the extinction at Gyanyima is 88 ky, which agrees well with estimates for the extinction interval of 60 ky proposed by Burgess et al. (2014), 83 ky by Wu et al. (2013) and of less than 200 ky by Shen et al. (2011). Thus, the fauna at Gyanyima confirms that the end Permian mass extinction was a geologically brief event.

5.2. Microstructures

Taxa belonging to the Order Productida show a laminar secondary layer where individual laminae are cross-bladed and 0.1–0.8 μm thick (Fig. 3A). In *Costiferina* sp. ind., the laminae consist of single blade/lath that are 1.5–2 μm wide and are crossed by broad pseudopunctae with taleolae at the core (Fig. 3B). The considerable thickness of the species of *Costiferina* (i.e., *C. indica*) is achieved by secretion of a large number of packed laminae and not by the formation of a prismatic layer. *Richthofenia lawrenciana* has a laminar shell crossed by a large number of small pseudopunctae (Fig. 3C). Taxa belonging to the order Spiriferida have a secondary layer made of fibers with typical keel and saddle morphology (Fig. 3D), and sometimes associated with a prismatic tertiary layer (Fig. 3E). The Orthida have an endopunctate fibrous secondary layer, but no tertiary layer (Fig. 3F). Among the Rhynchonellida, *Stenoscisma* sp. ind. possesses a shell with a secondary layer – of keel and saddle fibers - and a prismatic tertiary layer.

To evaluate the preservation of the original fabric, we make reference to Samtleben et al. (2001) and Garbelli et al. (2012), who assessed preservation by clustering microstructure into different morphotypes, based on the fabric of each layer, the morphology of the laminae, and the shape of individual fibers and/or prisms. Evaluation of the type of preservation for each shell analyzed by SEM is presented in Table 1 and summarized in Appendix 2.

312 **5.3. Cathodoluminescence**

313 To inspect the degree of diagenetic preservation/alteration of brachiopod low-Mg
314 calcite, shells were analyzed by cathodoluminescence, a tool that easily discriminates
315 post-depositional processes driven by meteoric fluid alteration. Calcite luminescence is
316 governed by the molar ratio of Fe/Mn. High Mn content in the calcite lattice induces
317 luminescence of the sample, whereas Fe is a quencher of luminescence in calcite (Machel
318 et al., 1991; Machel, 2000). Mn is generally low (<200 ppm) in unaltered recent and fossil
319 brachiopod shells (e.g., Brand et al., 2003), but it may be included in the calcite lattice
320 during post-depositional diagenetic processes (Brand and Veizer, 1980).
321 We observed a number of different patterns of luminescence in our samples:

322 (1) Non-luminescent shells with some thin, faint luminescent bands (laminar fabric);
323 also these shells may have some fractures filled with brightly luminescent material
324 (Figs. 4A, 4B);

325 (2) Non-luminescent shells, which are uniformly dark (fibrous fabric); sometimes the
326 outer part of these shells shows faint to moderate luminescence; occasionally their
327 fractures are filled by luminescent diagenetic calcite (Figs. 4D, 4F, 4M);

328 (3) Slightly to moderately luminescent shells (all fabrics) (Figs. 4C, 4N);

329 (4) Non-luminescent shell with punctae filled by luminescent diagenetic calcite
330 (punctate fibrous fabric) (Fig. 4I, 4L).

331 In general, brachiopods of the Gyanyima section are mainly non-luminescent of types 1
332 and 2 (Appendix 2). Cathodoluminescence discloses the presence of dull luminescent
333 cement filling some shells and/or fractures (Figs. 4F, 4I, 4N), and in a few shells dolomite
334 (Fe-rich, zoned) crystals, locally, replace the inner part of the tertiary layer (Fig. 4H).

335 **5.4. Trace elements and stable isotopes**

The subset analyzed for trace elements shows that all the brachiopod low-Mg calcite has low Mn content (Appendix 3). Except for one specimen (PTT-38-1), in which Mn contents reach 130 ppm, all other samples have Mn <100 ppm and in most cases it is < 50 ppm (Appendix 3). Mn contents are much higher in the coeval whole rock and may reach up to 1192 ppm. Fe content ranges from 5 to 285 ppm in the brachiopod shells, and from 71 to 361 ppm in the enclosing rock. Sr content of brachiopod low-Mg calcite ranges from 78 to 694 ppm, but laminar shells have higher values than fibrous ones with a maximum of only 430 ppm. The whole-rock samples have Sr contents between 82 and 293 ppm, with only two samples higher than 150 ppm (PPT-7-16m, PTT-8-14m). Mg contents range from 898 to 5136 ppm, but only three samples (PTT-16-4, PTT-37-3, PTT-38-4) have very high value up to 18,745 ppm. The rock matrix has a wide range from 2312 to 57,812 ppm Mg (Appendix 3). The $\delta^{13}C$ and $\delta^{18}O$ values of shells (preserved and altered) range from +1.85 to +6.30 ‰ and from -12.26 to -2.19 ‰, respectively (Appendix 3). Whole-rock $\delta^{13}C$ and $\delta^{18}O$ values range from +1.87 to +3.40 ‰ and from -9.35 to -2.37 ‰, respectively (Appendix 3).

5.5 Strontium isotope, ΣREE and Ce*

The $^{87}Sr/^{86}Sr$ ratio of all brachiopods (preserved and altered) ranges from a low value of 0.706958 to a high one of 0.707370, which are generally within the range of those reported for late Permian seawater (Appendix 3; Veizer et al., 1999). The ΣREE of the brachiopods ranges from 2.2 to 13.5 ppm, which brackets the values documented for modern and fossil shells with minimum alteration (Azmy et al., 2011, 2012; Brand et al., 2012a), and the whole rock ΣREE data from Tibet ranges from 10.6 to 94.9 ppm. The Ce/Ce* anomaly values (De Baar et al., 1988; Bau and Dulski, 1996; Azmy et al., 2011, 2012, Brand et al., 2012a) for the brachiopods ranges from 0.310 to 0.578, which is matched by the Ce/Ce* values of the enclosing rock ranging from 0.237 to 0.655 before the event, and of 0.276 for whole rock in the estimated extinction interval (Appendix 3). No

statistical difference at the 95 % confidence level was found between the brachiopods and coeval whole rock from Tibet (p= 0.775; Table 2).

6. Screening Process

6.1. Microstructure pattern and preservation of shells

Brachiopod shells of the Gyanyima Formation generally show good preservation of their microstructure, even in cases with site specific and selective alteration. Single shells with laminar and fibrous secondary fabrics may display selective preservation of the original fabric, with some regions having a pristine and well-defined texture, whereas others are altered. This is readily observed in species with thick laminar shells such as those of *Costiferina*, where the outer shell lost its original fabric, but the inner one did not (Fig. 3A). Similarly, some shells of species of *Permophricodothyris* have a slightly altered fibrous secondary layer, whereas the inner tertiary prismatic layer is pristine (e.g., Azmy et al., 2006). In some specimens, the alteration proceeds in such a differential way that the fibrous layer is totally lost, but the inner prismatic layer maintains even fine details, such as growth bands.

Overall, diagenetic alteration differentially affected the shell fabric, with the laminar one frequently more altered than the fibrous or prismatic ones. This may be related to differences in texture and size of the structural units forming the shells, resulting in a different arrangement of the organic matter in the biocomposites (Garbelli et al., 2014). In fact, approximately 70% of fibrous shells are morphologically preserved, in contrast to less than 30% preservation of laminar ones. Interestingly, morphological alteration is quite evident in laminar shells of unit 9 of the Gyanyima section (Fig. 2), while no alteration trend is observed in their fibrous shell counterparts.

6.2. Cathodoluminescence

Luminescence is another tool for evaluating the preservation of shells. Most of our specimens exhibit dull or no luminescence indicating good preservation of the brachiopod

low-Mg calcite. Dull luminescence, in many cases, indicates relative preservation of geochemical signature although altered carbonates might still exhibit no luminescence due to high Fe contents (Rush and Chafetz, 1990) and the degree of carbonate luminescence, therefore, must be interpreted with caution. The two types of shell succession display a different pattern of luminescence related to their different modality of alteration. Diagenetic fluids may seep more readily through the laminar fabric than through the fibrous layer (Fig. 4D, 4N), because the former is more porous (Garbelli et al., 2012). The low porosity of the secondary layer also results in the prismatic layer of Rhynchonellata being mostly non-luminescent, as they are less affected by Mn-enriched diagenetic fluids. Furthermore, other specific shell characteristics play a role in highlighting luminescence patterns, for example, the presence of dense pseudopunctae in *R. lawrenciana* produces inception horizons where fluids can easily infiltrate. In a similar way, punctae in fibrous fabrics leave voids after decomposition of the organic component, which may be filled later by luminescent diagenetic calcite (Fig. 4I, 4L).

Besides these fabric-controlled patterns, some shells show bright luminescence of the outermost layer (Figs. 4B, 4M), indicating that alteration driven by Mn-enriched diagenetic fluids was not strong enough to penetrate into the shell interior. In contrast, whole rock shows a broader range of luminescence due to the greater water/rock interaction ratio affecting the enclosing rock (Brand, 2004; Brand et al., 2012b). Whole rock from unit 9 contains euhedral, porphyritic dolomite crystals typical of an advanced degree of diagenesis corresponding to shallow burial (e.g., Haas et al., 2014) and high water-rock ratios (Banner and Hanson, 1990; Fig. 4C, 4H, 4M).

6.3 Evaluation of trace elements

Trace element contents are another tool for screening diagenetic overprints that may obscure the primary seawater signature in brachiopod low-Mg calcite. Comparing the geochemistry of brachiopod shells with that of coeval whole rock is a good test to evaluate

414 the influence of diagenetic alteration (e.g., Azmy et al., 2011, 2012; Brand et al., 2012b).
415 Furthermore, we do not apply static threshold values for trace elements, but select the
416 preserved brachiopod low-Mg calcite based on a comparison of the geochemistry with
417 other screening results as well as with the enclosing rock for each individual bed/horizon
418 (cf. Brand, 2004; Ullman and Korte, 2015).

419 Mn and Fe values show that most of the analyzed brachiopods did not undergo
420 alteration. More than 90% of the investigated shells have Mg values ranging from 1591 to
421 4000 ppm, a narrow and low range compared to that of the whole rocks. Some
422 brachiopods exceed those values and Mg content may reach up to 18,745 ppm. These
423 anomalous values are recorded by some specimens from unit 9 and are coupled with
424 negative $\delta^{18}O$ values (Appendix 3). Cathodoluminescence revealed that, in this
425 stratigraphic unit, rock matrices and brachiopod shells were locally dolomitized (Figs. 4H,
426 4M). This is consistent with the negative association between Mg and Sr (Fig. 5A, C).
427 Modern brachiopods from a variety of depositional environments have Sr contents of 450–
428 1928 ppm (Brand et al. 2003); diagenetic recrystallization of brachiopod low-Mg calcite
429 leads to depletion of Sr, but enrichment of Mg, Mn and Fe (Brand and Veizer, 1980;
430 Veizer, 1983; Banner and Hanson, 1990).

431 In comparison to modern brachiopods, the Sr values of the Tibet brachiopods fall in
432 the low range and sometimes exceed the lower threshold of 350 ppm. However, Sr in
433 brachiopod low-Mg calcite is tied to the Sr/Ca ratio of the seawater in which they thrived. In
434 Permian seas (Hardie, 1996; Stanley, 2006), the preferred carbonate phase was
435 aragonite, which is a more effective sink for seawater Sr than calcite (Stanley 2006).
436 Accordingly, the Sr/Ca ratios of seawater and calcite are inferred to have been low during
437 the Permian, when Sr-enriched aragonite was the preferred precipitate (Steuber and
438 Veizer, 2002). Hence, the low Sr content in the brachiopod low-Mg calcite is most likely

due to shells secreted in seawater with low Sr/Ca ratios rather than diagenetic alteration, which is consistent with the shell preservation (fibrous/laminated calcite prisms, dull CL and preserved ultrastructure under SEM). In fact, low Sr contents have been documented for Permian brachiopod shells in earlier studies (e.g., Joachimski et al., 2005), making it difficult to apply strict cut-off values extrapolated from modern datasets to evaluate diagenetic overprinting of Sr contents. The relationship between Sr/Ca ratios and contents of other minor elements (e.g., Fe, Mn, and Mg) seems to be a very effective tool to discriminate between pristine and altered brachiopod low-Mg calcite.

6.4. Stable isotope Screening

The degree of alteration for $\delta^{13}C$ and $\delta^{18}O$ in biogenic calcite are not always of similar magnitude, with a major role played by the isotopic composition of the post-depositional fluid and the environment of the fluid-rock system (Brand and Veizer, 1981; Banner and Hanson, 1990; Angiolini et al., 2012; Brand et al., 2011, 2012b). This type of differential alteration is clearly documented by the results – brachiopod and whole rock – from the Gyanyima section of Tibet (see for instance the results for the horizons 6-1 and 7-1 in Fig. 5B, D). The trends depicted by the carbonates in Figure 5 underscore the need for diagenetic screening at the horizon level, not on a collective scale that would miss subtle changes in isotopic compositions (cf. Brand, 2004; Brand et al., 2012b). All samples and results ($\delta^{13}C$, $\delta^{18}O$, $^{87}Sr/^{86}Sr$ and temperatures) that are deemed altered by the screening process are reported in red font in Appendix 3, consequently, only the results deemed pristine will form the basis for the following discussion.

7. Paleoceanography and paleoclimate of seamount Tibet

7.1 Chemical Paleoceanography

Strontium isotopes and REEs are powerful proxies, if preserved in archives, of oceanic and redox processes (e.g., Elderfield, 1981, 1990; Azmy et al., 2011; Azmy et al.,

2012; cf. Brand et al., 2012a; Zaky et al., 2015). The Sr isotope ratios of the brachiopods from units 1 through 8 vary from 0.706983 to 0.707056 and it is essentially invariant until the upper part of unit 8, where the ratio becomes more radiogenic, rising from 0.707023 to 0.707244 (Fig. 6). The $^{87}Sr/^{86}Sr$ trend for units 8 and 9 is similar to that recorded by whole rock data at Meishan, South China, although the values obtained from the pristine Gyanyima brachiopods are less radiogenic (Kaiho et al., 2001; Cao et al., 2009; cf. fig. 11, Brand et al., 2012a). In contrast, the $^{87}Sr/^{86}Sr$ recorded by the brachiopods from Sass de Putia and Val Brutta in the Dolomites of northern Italy (Brand et al., 2012a) is similar in trend and absolute values to that from Tibet. However, whole rock $^{87}Sr/^{86}Sr$ results from Iran (Liu et al., 2013) show a trend different from most other localities, posing questions about the reliability of $^{87}Sr/^{86}Sr$ values obtained from whole rock (cf. Brand, 2004; Brand et al., 2012a).

The Ce/Ce* anomaly values for the brachiopod shells and whole-rock samples are considered as one trend (Table 2) since they are not significantly different at the 95% confidence interval (brachiopods: N=13, mean 0.3763 ±0.1019; whole rock: N=38, mean 0.3859 ±0.1112; $p = 0.776$; cf. Zaky et al., 2015), and strongly suggest that seawater about the Tibetan seamount was oxic right up to and during the estimated extinction interval (Fig. 6; De Baar et al., 1988; Bau and Dulski, 1996). This is in agreement with the findings of Zhao et al. (2013), who, based on conodonts, show Ce/Ce* at Meishan being less than 1.0 from Bed 24 to Bed 26, thus indicating oxic water conditions across the event; with those of Loope et al. (2013), who found rare earths and yttrium (REY), iodine concentrations indicative of oxygenated seawater before and after the extinction event in Cili, South China. In contrast, the Ce/Ce* anomaly values of brachiopods and whole rock from northern Italy, Croatia, Slovenia, Austria, India and Meishan D of China (Brand et al., 2012a; Fio et al., 2010; Dolenec et al., 2001; Attrep et al., 1991; Algeo et al., 2007; Zhou and Kyte, 1988) are much more variable. It clearly suggests that open ocean seawater of

490 the southern Neotethys about the Tibet seamount was consistently oxic leading up to the
491 end Permian mass extinction, whereas in other more restricted localities, redox may have
492 been controlled by local conditions (cf. Brand et al., 2009, 2012a; Zaky et al., 2015).

493 **7.2 Paleoclimatology and SST**

494 Interpretation of the $\delta^{13}C$ and $\delta^{18}O$ record in terms of secular changes related to
495 environmental and climate variation is complex, and should be based on isotope data from
496 samples deemed to be pristine proxy according to exhaustive and multiple screening tests
497 (SEM, CL, TE and SI) and from well-constrained environmental settings.

498 Shen et al. (2010, fig. 6) published $\delta^{13}C$ values from whole rock of the Gyanyima
499 Formation through the Permian-Triassic boundary, but brachiopod shells are more reliable
500 archives of carbon and, especially oxygen isotope compositions (cf. Brand and Veizer,
501 1980; Brand, 2004; Brand et al., 2012b). However, since brachiopods do not range
502 stratigraphically into the end Permian event strata, we report both sets of data (Fig. 6;
503 Appendix 3). The preserved brachiopod low-Mg calcite has a range of $\delta^{13}C$ between 1.85
504 and 5.69 ‰, with more negative values recorded in laminar shells of Strophomenata than
505 in fibrous ones of the Rhynchonellata (Fig. 7). To standardize isotopic differences related
506 to the fabric a correction of +2.0 ‰ was applied to the $\delta^{13}C$ values of laminar shell
507 Strophomenata, considering that laminar fabric usually shows lighter values than co-
508 occurring fibrous ones (Garbelli et al., 2014), and we show the unadjusted as well as
509 adjusted results in Figure 8. After the adjustment, the carbon isotope curve displays a
510 generally steady value of $\delta^{13}C$ fluctuating between 4.04 ‰ and 5.60 ‰, with an overall
511 mean of 4.63 ‰. The adjusted $\delta^{13}C$ of brachiopod calcite is approximately 2.5 ‰ more
512 positive than the average value of the coeval whole rock reported by Shen et al. (2010,
513 figs. 6 and 9) and in this study, and differences in the overall trend can be seen throughout
514 the curve of the upper part (horizon 7-16 to 9-27) of the section at Gyanyima (Fig. 8). The
515 steady positive values of $\delta^{13}C$ up to unit 9 may be related to oceanographic processes. We

516 recognize that waters off the Tibet block were washed by warm and cool currents,
517 respectively carrying larvae of Paleotethyan taxa mixing with peri-Gondwanan ones (Shen
518 et al., 2010; Wang et al., 2010); thus at this convergence of warm and cool waters –
519 seawater productivity kicks into high gear producing DIC with highly positive $\delta^{13}C$ values.
520 In the upper part of unit 10, whole-rock samples record a slight negative shift in $\delta^{13}C$
521 (Fig. 8; Shen et al., 2010, fig. 6). Above, in the extinction horizon values increase and then
522 show a mild depletion in the Lower Triassic beds. The lack of a negative carbon isotope
523 excursion in brachiopods before and in whole rock before and during the event may reflect
524 diagenesis and/or different mineralogical fractionation since the analysis was done on
525 coral, sponge, echinoderm and algal grainstone, packstone and wackestone, not on pure
526 micrite or single brachiopod shells. To be noted that carbon isotopes from whole rock of
527 other Paleotethyan sections as those from North Iran (Gaetani et al., 2009, Schobben et
528 al. 2014) show variable excursions ranging from ~ 1‰ to more significant shifts of > 2 ‰.
529 The lack of a negative carbon isotope excursion (nCIE) normally associated with the end
530 Permian event should be taken as a sign of caution by all, considering the complicated
531 nature of the carbon cycle and thus its expression in carbonate rocks and allochems.
532 Therefore, we advise to consider detailed diagenetic and biologic screening of rock
533 material spanning this and other important biotic events.
534 Brachiopod $\delta^{18}O$ values show an evident trend of depletion in units 8 and 9 (Fig. 6).
535 In fact, starting from the base of Gyanyima Formation and up to 44 meters below the
536 Permian-Triassic boundary (base of unit 8), $\delta^{18}O$ values range from -3.26 ‰ to -2.72 ‰
537 (Table 3). In the overlying unit 8 there is a negative shift of about 2 ‰ (Fig. 6, Table 3),
538 and in unit 9, at 13 meters below the Permian-Triassic boundary $\delta^{18}O$ dramatically drops
539 down to -6.01 ‰.
540 We calculated seawater temperatures from these oxygen isotope data, applying the
541 oxygen isotope equation for synthetic calcite (Kim and O'Neill, 1997) and a recently

published oxygen isotope equation for brachiopod calcite (Brand et al., 2013). We also considered: 1) a seawater $\delta^{18}O$ of +0.7 ‰ based on clumped isotopes of brachiopods from northern Italy (Brand et al., 2012a; Came et al., 2014), and 2) seawater $\delta^{18}O$ of 0.0 and -0.5 ‰ for essentially ice-free subtropical latitudes during the Changhsingian (cf. Racki and Wignall, 2005; Fielding et al., 2008). The results are presented in Table 3.

Seawater temperatures, based on $\delta^{18}O$ data from brachiopod low-Mg calcite, in the southern Neotethys Ocean (southwestern Tibet) during the Late Permian fluctuated from 23.2 to 31.8°C, before the extinction event (Fig. 8, Table 3). This is consistent with the depositional environment of the Gyanyima Formation, which comprises subtidal reefal limestone of subtropical latitude in the southern Neotethys Ocean, but washed by warm Paleotethyan currents (Wang et al., 2010). Water temperatures at a depth of 10-15 m off Bermuda (in modern subtropical latitude) have a monthly range from 18.0 °C to 28.9°C and an annual average range of 22.4° to 24.3°C (Goodkin et al., 2008). Although, the temperature range obtained from Gyanyima brachiopods is about 4°C warmer than their modern counterparts off Bermuda, both are testimonials to their subtropical climates. This is also consistent with the climate models suggested for Late Permian oceans (e.g., Kiehl and Shields, 2005), which should have been warmer than present-day oceans.

The situation changes in the upper part of the Gyanyima Formation, where there is first an increase in temperature up to 32.6°C in unit 8, about 38 m below the PTB; seawater temperatures remained high up to unit 9, where a second increase in temperature exceeding 35°C is recorded from 13 to 9.5 m below the PTB. Considering constant sedimentation rates of ~ 121 m per million years, the highest temperature recorded in unit 9 occurred about 120 ky before the position of the Permian-Triassic boundary (Fig. 8). Thus, the increase in seawater temperature precedes the extinction event, as already suggested by Joachimski et al. (2012), and by Brand et al. (2012a). However, there is uncertainty in preservation and equilibrium of conodont apatite and,

568 unfortunately, brachiopod species at Gyanyima above unit 9 are not preserved to
569 comment on the subsequent evolution of Neotethys seawater temperature.

570 $\delta^{18}O$ of the brachiopods from unit 8 and in the lower part of unit 9 do not record the
571 cooling event envisaged by Shen et al. (2010) based on brachiopod associations, which
572 was not however recorded by the associated foraminiferal assemblages (Wang et al.,
573 2010). Consequently, the occurrence of peri-Gondwanan brachiopod taxa in this interval
574 may be related to larval transport by currents rather than to a temporary cooling event.
575 In order to compare our data from the subtropical setting of Gyanyima with that of
576 paleo-equatorial localities in the Late Permian, we recalculated seawater temperatures
577 from Sass de Putia and Tesero (Dolomites, N Italy; Brand et al., 2012a), using the recently
578 published oxygen isotope equation of Brand et al. (2013). The average background
579 temperature before the events appears to be slightly lower than previously assessed at 28-
580 32°C, but remains higher than present equatorial seawater temperature, which ranges
581 from 24 to 29°C (Jimenez, 2001; Colin, 2002; Brand et al., 2013). As a consequence, in
582 the Late Permian, the difference in seawater temperatures between an equatorial
583 restricted environment (Dolomites, northern Italy) and a subtropical open-ocean one
584 (Gyanyima, Tibet) was approximately 4°C. Interestingly, closer to the event the
585 background temperature difference of 4°C between equatorial and subtropical seawaters
586 disappears (Fig. 8). This is in agreement with models of global warming, predicting that
587 initial warming is faster at mid and high latitudes in comparison to those of tropical settings
588 (e.g., Brand et al., 2014), but later on differences in temperature along latitudes or different
589 environments become less marked with time (Kiehl and Shields, 2005).
590 The subtropical climate conditions for the Gyanyima Formation agree with records
591 from other uppermost Permian successions (Kearsey et al., 2009; Brand et al., 2012a;
592 Joachimski et al., 2012; B. Chen et al., 2013, Schobben et al., 2014) and they have been
593 interpreted as caused by the emission of the huge quantity of greenhouses gases by the

Siberian Traps (e.g.,Reichow et al., 2009; Svensen et al., 2009; Grasby et al., 2011; Brand et al., 2012a; Burgess et al., 2014). It is unequivocal, based on several biotic archives and geochemical proxies from a number of localities, that end Permian global warming started prior to the mass extinction event, and was far-reaching throughout the Tethys.

8. Conclusions

The end Permian mass extinction reached all corners of the globe including the seamount of Gyanyima, Tibet in the southern Neotethys. The geochemistry of pristine brachiopods from the open-sea Gyanyima Formation provides valuable insights into the oceanographic conditions of the Neotethys before the onset of the end-Permian mass extinction event:

1) After intensive and detailed screening of all available material (brachiopod shells and whole-rock samples) we re-constructed high-resolution strontium, carbon, redox and temperature curves for the subtropical latitude, open sea of the southern Neotethys during the Late Permian.
2) Ce/Ce* anomaly of brachiopods (0.310 to 0.577) and whole rock (0.237 to 0.655) before and in whole rock (0.276) during the estimated extinction interval suggests that the southern Neotethys seawater was oxic, which is well in agreement with modern counterparts and suitable for its rich invertebrate fauna.
3) $\delta^{13}C$ from brachiopod shells displays generally invariant values fluctuating between 4.04 ‰ and 5.60 ‰ up to unit 9, while two whole rock samples from unit 10 record a mild negative excursion before the Permian-Triassic boundary, which is ascribed to diagenesis.
4) Based on pristine brachiopod $\delta^{18}O$ and a seawater $\delta^{18}O$ composition of -0.5 ‰, seawater temperature at coral reef depth varied about 26°C from unit 1 to the base of unit 8 of the Gyanyima Formation. Subsequently, temperature of southern Neotethys seawater exceeded 35°C at about 120 ky before the Permian-Triassic boundary, just prior to the extinction event, which is similar to the seawater

temperatures recorded in northern Italy during this time, supporting the paradigm that global warming must have been an important factor of the biotic crisis

5) The pristine brachiopod archive from the open-ocean seamount Tibet in the southern Neotethys Ocean supports subtropical oceanic conditions right before the biotic event, but was followed by extreme warming to levels similar to those experienced at equatorial end Permian localities.

Acknowledgments

We thank M. Lozon (Brock University) for drafting some of the figures. We acknowledge C. Malinverno (Milan), A. Rizzi (Milan) and Yan Fang (Nanjing) for technical assistance. We thank Professor Steve C. Wang (Swarthmore College) for providing the algorithm for calculating the confidence interval for mass extinction duration.
We thanks two anonymous reviewers for their detailed revision and constructive criticism. We also acknowledge NSERC (#7961 to UB), NSFC (to SS), NSFC and MST of China (41290260 and 2011CB808900 to SSZ and CCQ), Brock University (to UB), Memorial University and PEEP (to KA), the Ferrara University (to RP), the MIUR (SAF/CHINA-2011 to CG), and the 2011 Italian Ministry PRIN Project "Past Excess CO_2 worlds: biota responses to extreme warmth and ocean acidification" to E. Erba (to CG and LA) for financial support.

References

Algeo, T.J., Hannigan, R., Rowe, H., Brookfield, M., Baud, A., Krystyn, L., Ellwood, B.B., 2007. Sequencing events across the Permian–Triassic boundary, Guryul Ravine (Kashmir, India). Palaeogeography, Palaeoclimatology, Palaeoecology 252, 328–346.

Angiolini, L., Checconi, A., Gaetani, M., R. Rettori, R., 2010. The latest Permian mass extinction in the Alborz Mountains (North Iran). Geological Journal 45, 216–229.

Angiolini, L., Stephenson, M.H., Leng, M.J., Jadoul, F., Millward, D., Aldridge, A., Andrews, J.E., Chenery, S., Williams, G., 2012. Heterogeneity, cyclicity and diagenesis in a Mississippian brachiopod shell of palaeoequatorial Britain. Terra Nova 24, 16–26.

650 Attrep Jr.M., Orth, C.J., Quintana, L.R., 1991. The Permian-Triassic of the Gartnerkofel-1 Core
651 (Carnic Alps, Austria): Geochemistry of Common and Trace elements II: INAA and RNAA.
652 Abhandlungen der Geologischen Bundesanstalt, 45, 123-137.

653 Azmy, K., Veizer, J., Jin, J., Copper, P.,Brand, U., 2006. Paleobathymetry of a Silurian shelf:
654 oxygen isotope test. Canadian Journal of Earth Sciences, 43: 281–293

655 Azmy, K., Brand, U., Sylvester, P., Gleeson, S.A., Logan, A., Bitner, M.A., 2011. Biogenic and
656 abiogenic low Mg calcite (bLMC and aLMC): evaluation of seawater-REE composition, water
657 masses and carbonate diagenesis. Chemical Geology 280, 180–190

658 Azmy, K., Poty, E., Mottequin, B., 2012. Biochemostratigraphy of the Upper Frasnian in the
659 Namur-Dinant Basin, Belgium: implications for a global Frasnian-Famennian pre-event.
660 Palaeogeography, Palaeoclimatology, Palaeoecology, 313-314: 93-106.

661 Banner, J.L., Hanson, G.N., 1990. Calculation of simultaneous isotopic and trace element
662 variations during water-rock interaction with applications to carbonate diagenesis. Geochimica
663 et Cosmochimica Acta, 54, 3123-3137.

664 Bau, M., Dulski, P., 1996. Distribution of yttrium and rare-earth elements in the Penge and
665 Kuruman iron-formations, Transvaal Supergroup, South Africa. Precambrian Research 79, 37-
666 55.

667 Birck, L.J., 1986. Precision K\Rb\Sr isotopic analysis: application to Rb\Sr chronology. Chemical
668 Geology 56 73–83.

669 Brand, U., 2004. Carbon, oxygen and strontium isotopes in Paleozoic carbonate components: an
670 evaluation of original seawater-chemistry proxies. Chemical Geology 204, 23-44.

671 Brand, U., Veizer, J., 1980. Chemical diagenesis of a multicomponent carbonate system:
672 1, Trace elements. Journal of Sedimentary Petrology 50, 1219–1236.

673 Brand, U., Veizer, J., 1981. Chemical diagenesis of a multicomponent carbonate system:
674 2, Stable isotopes. Journal of Sedimentary Petrology 51, 987-997.

675 Brand, U., Logan, A., Hiller, N., Richardson, J., 2003. Geochemistry of modern
676 brachiopods: applications and implications for oceanography and paleoceanography.
677 Chemical Geology, 198, 305-334.

678 Brand, U., Tazawa, J.I., Sano, H., Azmy, K., Lee, X., 2009. Is mid-late Paleozoic ocean-chemistry
679 coupled with epeiric seawater isotope records? Geology, 37, 823-826.

680 Brand, U., Logan, A., Bitner, M.A., Griesshaber, E., Azmy, K., Buhl, D., 2011. What is the
681 ideal proxy of Paleozoic seawater chemistry? Memoir of the Association of Australasian
682 Palaeontologists 41, 9–24.

683 Brand, U., Posenato, R., Came, R., Affek, H., Angiolini, L., Azmy, K., Farabegoli, E.,
684 2012a. The end-Permian mass extinction: a rapid volcanic CO2 and CH4-climatic
685 catastrophe. Chemical Geology 322–323, 121–144.

686 Brand, U., Jiang, G., Azmy, K., Bishop, J.W., Montanez, I.P., 2012b. Diagenetic evaluation
687 of a Pennsylvanian carbonate succession (Bird Spring Formation, Arrow Canyon,
688 Nevada, U.S.A.) — 1: Brachiopod and whole rock comparison. Chemical Geology, 308-
689 309, 26-39.

690 Brand, U., Azmy, K., Bitner, M.A., Logan, A., Zuschin, M., Came, R., Ruggiero, E., 2013.
691 Oxygen isotopes and MgCO3 in brachiopod calcite and a new paleotemperature
692 equation. Chemical Geology 359, 23–31.

693 Brand, U., Came, R.E., Affek, H., Azmy, K., Mooi, R., Layton, K., 2014. Climate-forced change in

694 Hudson Bay seawater composition and temperature, Arctic Canada. Chemical Geology,
695 388: 78-86.
696 Burgess, S.D., Bowring, S., Shen, S.-Z., 2014. High precision timeline for Earth's most
697 severe extinction. Proceedings of the National Academy of Sciences of the United
698 States of America 111, 3316–3321.

699 Came, R.E., Brand, U., Affek, H., 2014. Clumped isotope signatures in modern brachiopod
700 carbonate. Chemical Geology 377, 20-30.

701 Cao, C. et al., 2009. Biogeochemical evidence for euxinic oceans and ecological disturbance
702 presaging the end-Permian mass extinction event. Earth and Planetary Science Letters 281,
703 188-201.

704 Carpenter, S.J., Lohmann, K.C., 1995. Delta-O-18 and delta-C-13 values of modern brachiopod
705 shells. Geochimica et Cosmochimica Acta 59, 3749–3764.

706 Chen, B., Joachimski, M.M., Shen, S.Z., Lambert, L.L., Lai, X.L., Wang, X.D., Chen, J., Yuan,
707 D.X., 2013. Permian ice volume and palaeoclimate history: oxygen isotope proxies revisited.
708 Gondwana Research 24, 77–89.

709 Clarkson, M.O., Kasemann, S.A., Wood, R.A., Lenton, T.M., Daines, S.J., Richoz, S.,
710 Ohnemueller, F., Meixner, A., Poulton, S.W., Tipper, E.T., 2015. **Ocean acidification and the**
711 **Permo-Triassic mass extinction. Science 348, 229-232.**

712 Colin, P.L., 2002. Water temperatures on the Palauan Reef Tract: Year 2000. Coral Reef
713 Research Foundation, Koror.

714 Crasquin-Soleau, S., Shen, S.Z., Li, W.Z., Cao, C.Q., 2007. Ostracods from the Lopingian
715 and Permian–Triassic boundary beds at the Gyanyima section in southwestern Tibet,
716 China. Palaeoworld 16, 222–232.

717 Cusack, M., Perez-Huerta, A., EIMF, 2012. Brachiopods recording seawater
718 temperature—a matter of class or maturation? Chemical Geology 334, 139–143.

719 De Baar, H.J.W., German, C.R., Elderfield, H., van Gaans, P., 1988. Rare earth element
720 distributions in anoxic waters of the Curacao Trench. Geochimica et Cosmochimica Acta 52,
721 1203-1219.

722 Dolenec, T., Lojen, S., Ramovs, A., 2001. The Permian-Triassic boundary in western Slovenia
723 (Idrija Valley section): magnetostratigraphy, stable isotopes, and elemental variations.
724 Chemical Geology 175, 175-190.

725 Elderfield, H., Greaves, M.J., 1981. Strontium isotope geochemistry of Icelandic geothermal
726 systems and implications for sea water chemistry. Geochimica et Cosmochimica Acta 45,
727 2201-2212.

728 Elderfield, H., Upstill-Goddard, R., Sholkovitz, E., 1990. The rare earth elements in rivers,
729 estuaries and coastal sea waters: processes affecting crustal input of elements to the ocean
730 and their significance to the composition of sea water. Geochimica et Cosmochimica Acta 54,
731 971-991.

732 Erwin, D. H., 2006. Extinction: how life on earth nearly ended 250 million years ago.
733 Princeton University Press, Princeton, N.J.

734 Fielding, C.R., Frank, T.D., Birgenheier, L.P., Rygel, M.C., Jones, A.T., Roberts, J., 2008.
735 Stratigraphic imprint of the Late Palaeozoic Ice Age in eastern Australia: a record of
736 alternating glacial and nonglacial climate regime. Journal of the Geological Society 165,
737 129–140.

738 Fio, K., Spangenberg, J.E., Vlahović, I., Sremac, J., Velić, I., Mrinjek, E., 2010. Stable isotope

739 and trace element stratigraphy across the Permian–Triassic transition: a redefinition of the
740 boundary in the Velebit Mountain, Croatia. Chemical Geology 278, 38–57.

741 Gaetani, M., Angiolini, L., Ueno, K., Nicora, A., Stephenson, M.H., Sciunnach, D., Rettori, R.,
742 Price, G.D., Sabouri, J., 2009. Pennsylvanian–Early Triassic stratigraphy in the Alborz
743 Mountains (Iran). Geological Society, London, Special Publication 312, 79–128.

744 Garbelli, C., Angiolini, L., Jadoul, F., Brand, U., 2012. Micromorphology and differential
745 preservation of Upper Permian brachiopod low-Mg calcite. Chemical Geology 299, 1–
746 10.

747 Garbelli, C., Angiolini, L., Brand, U., Jadoul, F., 2014. Brachiopod fabric, classes and
748 biogeochemistry: Implications for the reconstruction and interpretation of seawater
749 carbon-isotope curves and records. Chemical Geology 371, 60-67.

750 Ghaderi, A., Leda, L., Schobben, M., Korn, D., Ashouri, A.R., 2014 High-resolution
751 stratigraphy of the Changhsingian succession of NW Iran and the Transcaucasus based
752 on lithological features, conodonts and ammonoids. Fossil record, 17, 41-57

753 Goodkin, N.F., Hughen, K.A., Curry, W.B., Doney, S.C., Ostermann, D.R. 2008.
754 Sea surface temperature and salinity variability at Bermuda during the end of the Little
755 Ice Age. Paleoceanography, 23 (3).

756 Grasby S.E., Sanei H., Beauchamp B., 2011. Catastrophic dispersion of coal fly ash into
757 the oceans during the latest Permian extinction. Nature Geoscience. 4(2), 104-107.

758 Guo, T.Y., Liang, D.Y., Zhang, Y.Z., Zhao, C.H., 1991. Geology of Ngari, Tibet (Xizang).
759 The China University of Geosciences Press, Wuhan. 464 pp. (in Chinese).

760 Haas, J., Budai, T., Gyori, O., Kele, S., 2014. Multiphase partial and selective
761 dolomitization of Carnian reef limestone (Transdanubian Range, Hungary).
762 Sedimentology 61, 836-859.

763 Hardie, L.A., 1996. Secular variation in seawater chemistry: an explanation for the coupled
764 secular variation in the mineralogies of marine limestones and potash evaporites over
765 the past 600 m.y. Geology 24, 279 – 283.

766 Isozaki, Y., 1997. Permo-Triassic superanoxia and stratified superocean: records from lost
767 deep sea. Science 276, 235‑238.

768 Jimenez, C. 2001. Seawater temperature measured at the surface and at two depths (7
769 and 12 m) in one coral reef at Culebra Bay, Gulf of Papagayo, Costa Rica. Revista de
770 Biologia Tropical 49, 153-161, Supplement 2.

771 Joachimski, M.M., Simon, L., van Geldern, R., Lécuyer, C., 2005. Boron isotope
772 geochemistry of Paleozoic brachiopod calcite: implications for a secular change in the
773 boron isotope geochemistry of seawater over the Phanerozoic. Geochimica et
774 Cosmochimica Acta 69, 4035–4044.

775 Joachimski, M.M., Lai, X., Shen, S., Jiang, H., Luo, G., Chen, B., Chen, J., Sun, Y., 2012.
776 Climate warming in the latest Permian and the Permian–Triassic mass extinction.
777 Geology 40, 195–198

778 Kaiho, K., Kajiwara, Y., Nakano, T., Miura, Y., Kawahata, H., Tazaki, K., Ueshima, M.,
779 Chen, Z.Q., Shi, G.R., 2001. End-Permian catastrophe by a bolide impact: evidence of
780 a gigantic release of sulfur from the mantle. Geology 29, 815–818.

781 Kearsey, T., Twitchett, R.J., Price, G.D., Grimes, S.T., 2009. Isotope excursions and
782 paleotemperature estimates from the Permian/Triassic boundary in the Southern Alps
783 (Italy). Palaeogeography, Palaeoclimatology, Palaeoecology 279, 29–40.

784 Kiehl, J.T., Shields, C.A., 2005. Climate simulation of the latest Permian: implications for
785 mass extinction. Geology 33, 757–760.

786 Kim, S.T., O'Neil, J.R., 1997. Equilibrium and non equilibrium oxygen isotope effects in
787 synthetic carbonates. Geochimica et Cosmochimica Acta 61, 3461–3475.

788 Korte, C., Jasper, T., Kozur, H.W., Veizer, J., 2005. $\delta^{18}O$ and $\delta^{13}C$ of Permian
789 brachiopods: a record of seawater evolution and continental glaciation.
790 Palaeogeography, Palaeoclimatology, Palaeoecology 224, 333–351.

791 Leng, M.J., Marshall, J.D., 2004. Palaeoclimate interpretation of stable isotope data from
792 lake sediment archives. Quat. Sci. Rev. 23, 811–831.

793 Liu, X.C., Wang, W., Shen, S.Z., Gorgij, M.N., Ye, F.C., Zhang, Y.C., Furuyama, S., Kano,
794 A., Chen, X.Z., 2013. Late Guadalupian to Lopingian (Permian) carbon and strontium
795 isotopic chemostratigraphy in the Abadeh section, central Iran. Gondwana Research
796 24,22-232.

797 Loope, G.R., Kump, L.R., Arthur, M.A., 2013. Shallow water redox conditions from the
798 Permian-Triassic boundary microbialite: The rare earth element and iodine
799 geochemeistry of carbonates from Turkey and South China. Chemical Geology 351,
800 195–208.

801 Lowenstam, H., 1961. Mineralogy, O18/O16 ratios, and strontium and magnesium contents of
802 recent and fossil brachiopods and their bearing on the history of the oceans. Journal of
803 Geology 69, 241-260.

804 Machel, H.G., 2000. Application of cathodoluminescence to carbonate diagenesis. In: Pagel, M.,
805 Barbin, V., Blank, P., Ohnenstetter, D. (Eds.), Cathodoluminescence in Geosciences. Springer,
806 New York, pp. 271–301.

807 Machel, H.G., Mason, R.A.,Mariano, A.N.,Mucci, A., 1991. Causes and emission of
808 luminescence in calcite and dolomite. In: Barker, C.E., Kopp, O.C. (Eds.),
809 Luminescence Microscopy and spectroccopy: qualitative and quantitative applications.
810 Short Course, 25. Society for Sedimentary Geology, Tulsa, pp. 9–25.

811 McArthur, J.M., Howarth, R.J., Bailey, T.R., 2001. Strontium isotope stratigraphy:
812 LOWESS version 3: best fit to the marine Sr-isotope curve for 0–509 Ma and
813 accompanying look-up table for deriving numerical age. Journal of Geology 109, 155–
814 170.

815 Meldahl, K. H. 1990. Sampling, species abundance, and the stratigraphic signature of
816 mass extinction: a test using Holocene tidal flat molluscs. Geology 18,890–893.

817 Muttoni, G., Gaetani, M., Kent, D.V., Sciunnach, D., Angiolini, L., Berra, F., Garzanti, E.,
818 Mattei, M., Zanchi, A., 2009a. Opening of the Neo-Tethys Ocean and the Pangea B to
819 Pangea A transformation during the Permian. GeoArabia 14, 17–48.

820 Parkinson, D., Curry, G.B., Cusack, M., Fallick, A.E., 2005. Shell structure, patterns and
821 trends of oxygen and carbon stable isotopes in modern brachiopod shells. Chemical
822 Geology 219, 193–235.

823 Payne, J.L., Clapham, M.E., 2012. End-Permian mass extinction in the oceans: an ancient
824 analog for the twenty-first century? Annual Review of Earth and Planetary Sciences 40,
825 89–111.

826 Racki, G., Wignall, P.B., 2005. Late Permian double-phased mass extinction and
827 volcanism: an oceanographic perspective. In: Over, D.J., Morrow, J.R., Wignall, P.B.

(Eds.), Understanding Late Devonian and Permian–Triassic biotic and climatic events: towards an integrated approach. Elsevier, pp. 263–297.

Reichow, M.K., Pringle, M.S, Al'Mukhamedov, A.I., Allen, M.B., Andreichev, V.L., Buslov, M. M., Davies, C.E., Fedoseev, G.S., Fitton, Godfrey, Inger, S., Medvedev, A.Y., Mitchell, C., Puchkov, V.N., Safonova, I.Y., Scott, R.A., Saunders, A.D., 2009. The timing and extent of the eruption of the Siberian Traps large igneous province: Implications for the end-Permian environmental crisis. Earth Planetary Science Letters 277(1-2):9–20.

Retallack, G.J., 2013. Permian and Triassic greenhouse crises. Gondwana Research 24, 90–103.

Rush, P.F., Chafetz, H.S., 1990. Fabric retentive, non-luminescent brachiopods as indicators of original $\delta^{13}C$ and $\delta^{18}O$ compositions: a test. Journal of Sedimentary Petrology 60, 968–981.

Samtleben, C.,Munnecke, A., Bickert, T., Patzold, J., 2001. Shell succession, assemblage and species dependent effects on C/O-isotopic composition of brachiopods – examples from the Silurian of Gotland. Chemical Geology 175, 61–107.

Schobben, M., Joachimski, M.M., Korn, D., Leda, L., Korte, C., 2014. Palaeotethys seawater temperature rise and intensified hydrological cycle following the end-Permian mass extinction. Gondwana Research 26, 675-683.

Signor, P. W., and J. H. Lipps. 1982. Sampling bias, gradual extinction patterns, and catastrophes in the fossil record. In L. T. Silver and P. H. Schultz, eds. Geological implications of large asteroids and comets on the Earth. Geological Society of America Special Paper 190, 291–296.

Shen, S.Z., Cao, C.Q., Shi, G.R., Wang, X.D., Mei, S.L., 2001. Lopingian (Late Permian) stratigraphy, sedimentation and palaeobiogeography in southern Tibet. Newsletters on Stratigraphy 39, 157–179.

Shen, S.Z., Sun, D.L., Shi, G.R., 2003. A biogeographic mixed late Guadalupian (late Middle Permian) brachiopod fauna from an exotic limestone block at Xiukang in Lhaze county, Tibet. Journal of Asian Earth Sciences 21, 1125–1137.

Shen S.Z., Cao C.Q., Henderson C.M., Wang X.D., Shi G.R., Wang Y., Wang W., 2006. End-Permian mass extinction pattern in the northern peri-Gondwanan region. Palaeoworld,15(1), 3-30.

Shen, S.Z., Cao, C.Q., Zhang, Y.C., Li, W.Z., Shi, G.R., Wang, Y., Wu, Y.S., Ueno, K., Henderson, C.M., Wang, X.D., Zhang, H., Wang, X.J., Chen, J., 2010. End-Permian mass extinction and palaeoenvironmental changes in Neotethys: evidence from an oceanic carbonate section in southwestern Tibet. Global and Planetary Change 73, 3–14.

Shen, S. Z., J. L. Crowley, Y. Wang, S. A. Bowring, D. H. Erwin, P. M. Sadler, C. Q. Cao, D. H. Rothman, C. M. Henderson, J. Ramezani, H. Zhang, Y. A. Shen, X. D. Wang, W. Wang, L. Mu, W. Z. Li, Y. G. Tang, X. L. Liu, L. J. Liu, Y. Zeng, Y. F. Jiang, and Y. G. Jin. 2011. Calibrating the end-Permian mass extinction. Science 334, 1367–1372.

Shen S.Z., Schneider J.W., Angiolini L., Henderson C.M. 2013. The International Permian timescale: March 2013 update. Lucas, S.G., et al. eds., 2013, The Carboniferous-Permian Transition. New Mexico Museum of Natural History and Science, Bulletin 60, 411-416.

874 Stanley, S.M. 2006. Influence of seawater chemistry on biomineralization throughout
875 Phanerozoic time: Paleontological and experimental evidence. Palaeogeography
876 Palaeoclimatology Palaeoecology 232, 214-236.

877 Steuber, T., Veizer, J., 2002. Phanerozoic record of plate tectonic control of seawater
878 chemistry and carbonate sedimentation. Geology 30, 1123–1126.

879 Svensen, H., Planke, S., Polozov, A.G., Schmidbauer , N., Corfu, F., Podladchikov, Y.Y.,
880 Jamtveit, B., 2009. Siberian gas venting and the end-Permian environmental crisis.
881 Earth Planetary Science Letters 277, 490–500.

882 Ullman, C.V., Korte, C., 2015. Diagenetic alteration in low-Mg calcite from macrofossils: a review.
883 Geological Quaterly, 59: 3-20.
884 Vachard, D., 2014. Colaniella, wrongly named, well-distributed Late Permian nodosariate
885 foraminifers. Permophiles 60.
886 Veizer, J., 1983. Trace elements and stable isotopes in sedimentary carbonates. In:
887 Reeder, R.J. (Ed.), Carbonates: Mineralogy and Chemistry. Mineralogical Society of
888 America, Blacksburg, pp. 265–299.

889 Veizer, J., Ala, D., Azmy, K., Bruckschen, P., Bruhn, F., Buhl, D., Carden, G., Diener, A.,
890 Ebneth, S., Goddris, Y., Jasper, T., Korte, C., Pawellek, F., Podlaha, O., Strauss, H.,
891 1999. 87Sr/86Sr, δ18O and δ13C evolution of Phanerozoic seawater. Chemical
892 Geology 161, 59–88.

893 Wang, Q.H., Xu, C.X., 1988. Permian strata in Gyanyima, Zanda, Tibet. Regional Geology
894 of China 1, 67–70.

895 Wang, S.C., Marshall, C.R., 2004. Improved confidence intervals for estimating the
896 position of a mass extinction boundary. Paleobiology 30, 5–18

897 Wang, S. C., A. E. Zimmerman, B. S. McVeigh, P. J. Everson, and H. Wong. 2012.
898 Confidence intervals for the duration of mass extinction. Paleobiology 38, 265–277

899 Wang, Y., Ueno, K., Zhang, Y.C., Cao, C.Q., 2010. The Changhsingian foraminiferal fauna
900 of a Neotethyan seamount: the Gyanyima Limestone along the Yarlung–Zangbo Suture
901 in southern Tibet, China. Geological Journal 45, 308–318.

902 Wu, H.C., Zhang, S.H., Hinnov, L.A., Jiang, G.Q., Feng, Q.L., Li, H.Y., Yang, T.S., 2013.Time-
903 calibrated Milankovitch cycles for the late Permian. Nature Communication 4, 2452.

904 Yamamoto, K., Asami, R., Iryu, Y., 2013. Correlative relationships between carbon- and
905 oxygen-isotope records in two cool-temperate brachiopod species off Otsuchi Bay,
906 northeastern Japan. Paleontological Research 17, 12–26.

907 Zaky, A., Brand, U, Azmy, K. 2015. A new sample processing protocol: an important
908 update to procuring reliable REE signatures. 7th International Brachiopod Congress,
909 Nanjing, China, May 22-25, 2015.

910 Zhao, L., Chen, Z.Q., Algeo, T.J., Chen, J., Chen, Y., Tong, J., Gao, S., Zhou, L., Hu, C.,
911 Liu, Y., 2013. Rare-earth element patterns in conodont albid crowns: evidence for
912 massive inputs of volcanic ash during the latest Permian biocrisis? Global and Planetary
913 Change 105, 135–151.

914 Zhou, L., Kyte, F.T., 1988. The Permian-Triassic boundary events: a geochemical study of three
915 Chinese sections. Earth and Planetary Science Letters 90, 411-421.

916

917 Figure captions

Fig. 1. Late Permian paleogeographic reconstruction showing the position of the Gyanyima block and of the Permian-Triassic boundary sections of the Dolomites (Italy) and Meishan (South China, red stars; modified after Muttoni et al. 2009). The inset provides greater detail of the geographic location of the Gyanyima section.

Fig. 2. Stratigraphic log showing the lithology and last occurrences of taxa in the Gyanyima Formation (modified after Shen et al. 2010). The range extensions (blue line) are calculated using the equation given by Strauss and Sadler (1989); the red line is the extinction boundary that lies above the highest fossil presence (Wang and Marshall, 2004) and below the first occurrence of Triassic conodonts, which is about 1.3 m above the base of the Lanchengquxia Fm. (Shen et al. 2010). The orange band indicates the extinction duration with a confidence interval of 95% following the methods of Wang et al. (2012) (Appendix 1A/B). On the right, the plot the stratigraphic abundance versus last occurrence below the extinction horizon shows that the extinction was sudden (Meldahl, 1990).

Figure 3. A - specimen 79 (8-14), laminar secondary layer of *Costiferina indica* with typical cross-bladed pattern; laminae are formed by structural units packed together with parallel longitudinal axes, organized in distinct packages, each with blade axis orientations approximately perpendicular to the adjacent one, as shown by the alternation of longitudinal (l) and cross (c) sections of the laminae; B - specimen 13 (7-5), details of a pseudopuncta of *Costiferina* sp. ind. formed by inwardly deflected laminae around a solid rod of calcite called taleola (t); C - specimen 52 (6-12), laminar secondary layer of *Richthofenia lawrenciana* crossed by numerous pseudopunctae (arrows); D - specimen 19 (9-23), cross section of fibers of the secondary layer of *Permophricodothyris* sp. ind. ind.; E - specimen 83 (T9-23), prismatic tertiary layer of *Permophricodothyris* sp. ind. ind. showing micrometric bands which represent steps of growth; F - specimen 41 (6-12), fibrous secondary layer of *Acosarina* sp. ind. crossed by endopunctae (sp) which deflect the fibers outward; G - specimen 77 (8-13), well preserved laminar secondary layer of *Costiferina indica* showing a fracture (arrows) filled by diagenetic calcite (outlined); H - specimen 70 (6-15), altered fibrous secondary layer of *Permophricodothyris* sp. ind. in which the fibers lose their outline and are partially amalgamated.

Figure 4. A - specimen 75 (8-2), laminar secondary layer of *Costiferina indica* showing pattern of non luminescent and faint luminescent bands; B - specimen 63 (6-12), laminar secondary layer of *Costiferina subcostatus* showing a slightly luminescent region external rim(sl), a non luminescent inner region (nl) and a fracture-filled luminescent diagenetic

calcite (arrow); C - specimen 86 (9-27), secondary shell of *Costiferina subcostatus* with a network of fractures filled by luminescent diagenetic calcite (arrow), crossing non luminescent shell (nl); the matrix (m) is luminescent; D - specimen 36 (9-23), non luminescent prismatic shell (s) of *Permophricodothyris* sp. ind.; E/F - specimen 48 (9-23), shell of *Stenoscisma* sp. ind. in transmitted light and cathodoluminescence respectively; the shell is non luminescent; the internal cavity is (s) filled by fibrous radial calcite cement (c) of three zones (c1, c2, c3); G/H - specimen 81 (9-23), shell of *Neospirifer* sp. ind. in transmitted light and cathodoluminescence respectively; the outer secondary layer (f) is slightly luminescent (sl) and the inner prismatic one (p) is non luminescent (nl) but partially dolomitized by luminescent zoned dolomite rhombs (d); I / L – specimen 58 (9-23), non luminescent fibrous secondary layer of *Notothyris* sp. ind. (s) crossed by endopunctae which are filled by luminescent diagenetic calcite and an internal cavity filled by diagenetic calcite with different zones of luminescence (c1, c2 and c3) similar to fig. F; M – specimen 37 (9-23), luminescent secondary (l) and non luminescent tertiary (nl) layers of *Permophricodothyris* sp. ind. with a few fractures (arrow) filled by diagenetic luminescent calcite and partially dolomitized matrix (m); N - specimen 78 (8-14), secondary laminar layer of *Costiferina indica* (s) showing alternation of luminescent and faint luminescent bands; the internal cavity is filled by calcite cements (c). In all figures (m) indicates the matrix.

Fig. 5. Strontium, magnesium, carbon and oxygen isotope trends with progressive post-depositional alteration in brachiopods and whole rock from Tibet. The depletion of Sr and enrichment of Mg is typical for post-depositional alteration in the presence of meteoric water (Brand and Veizer, 1980). Enrichment in the light carbon and oxygen isotope values depends on the isotopic composition of the diagenetic fluid (cf. Brand and Veizer, 1981; Banner and Hanson, 1990; Brand, 2004). Material from beds 6-1 (A, B) and 7-1 (C, D) show trends typical of diagenetic alteration; a screening concept applied to all horizons (Brand et al., 2011; Ullman and Korte, 2015).

Fig. 6. Chemostratigraphic and temperature trends for the Changhsingian succession of the Gyanyima Formation of seamount Tibet. The Sr isotope trend is invariant until the base of unit 8, subsequently values become increasingly radiogenic. Carbon isotope compositions are variable throughout the succession, but show no negative carbon isotope excursion, with whole rock values more negative by about 2‰ compared to brachiopod ones. Oxygen isotope compositions are equally invariant through units 6 and 7, followed

by negative excursions in units 8 and 9. Ce* anomaly values of brachiopods and whole rock are consistently less than unity and thus infer oxic seawater conditions throughout the sequence. Temperature is relatively invariant until the base of unit 8, but then it takes a dramatic and sudden leap to higher values. We present brachiopod $\delta^{13}C$ before (green empty symbols) and after (green filled symbols) adjustment for fabric control (see text; cf. Garbelli et al., 2014). Filled and cross symbols represent preserved and partially altered specimens respectively.

Fig. 7. Cross plot of $\delta^{13}C$ in Strophomenata and Rhynchonellata shells. It is evident that $\delta^{18}O$ composition of brachiopod taxa of the two classes has a similar range of values , whereas the δ13C composition is conspicuously different, as also highlighted by the box plots in the right corner. Filled, cross and empty symbols represent preserved, partially altered and altered specimens respectively.

Fig. 8. A close-up of the carbon, strontium and temperature trends from horizon 7-16 to 9-27 of the Gyanyima Formation of Tibet. Brachiopod and whole rock $\delta^{13}C$ is invariant right up to onset and into (only whole rock data) the end Permian mass extinction event. The slight negative excursion of $\delta^{13}C$ values noted in horizon T-10-40 and T-10-41. is ascribed to diagenetic alteration. In contrast, strontium isotopes and water temperature show significant radiogenic and positive (warming) offsets approaching the event. We present brachiopod $\delta^{13}C$ after adjustment for fabric control. Filled and cross symbols represent preserved and partially altered specimens respectively.

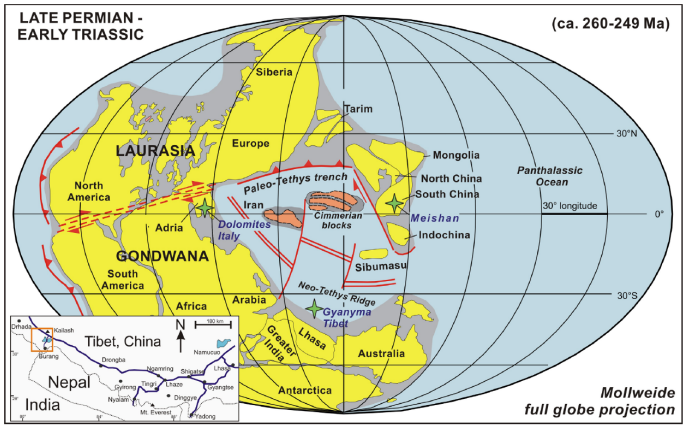

Figure 1

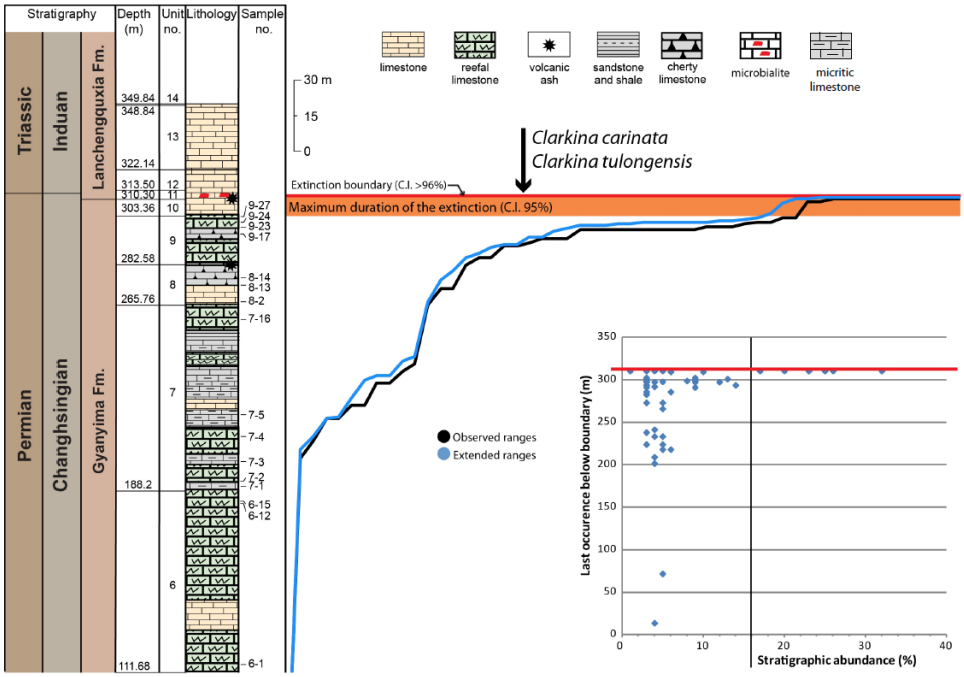

Figure 2

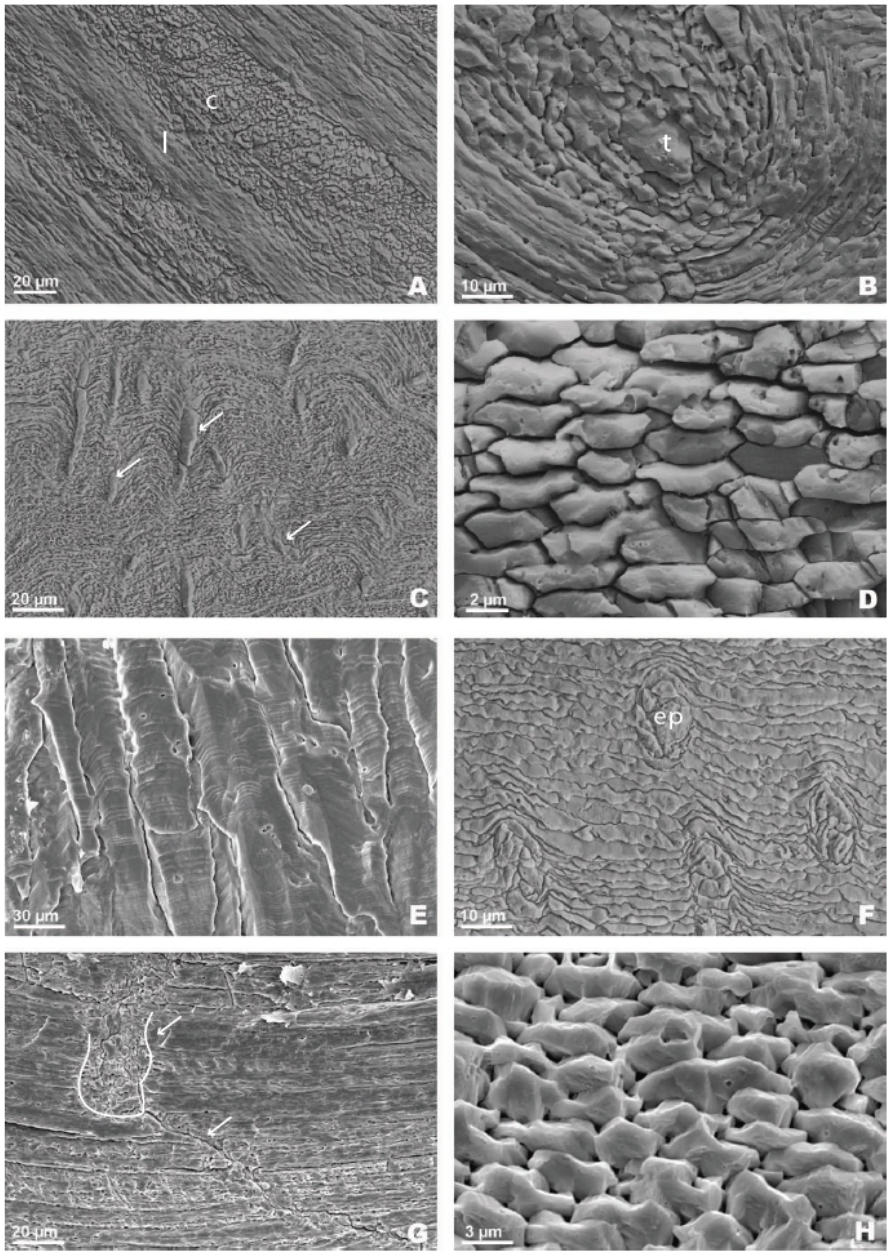

Figure 3

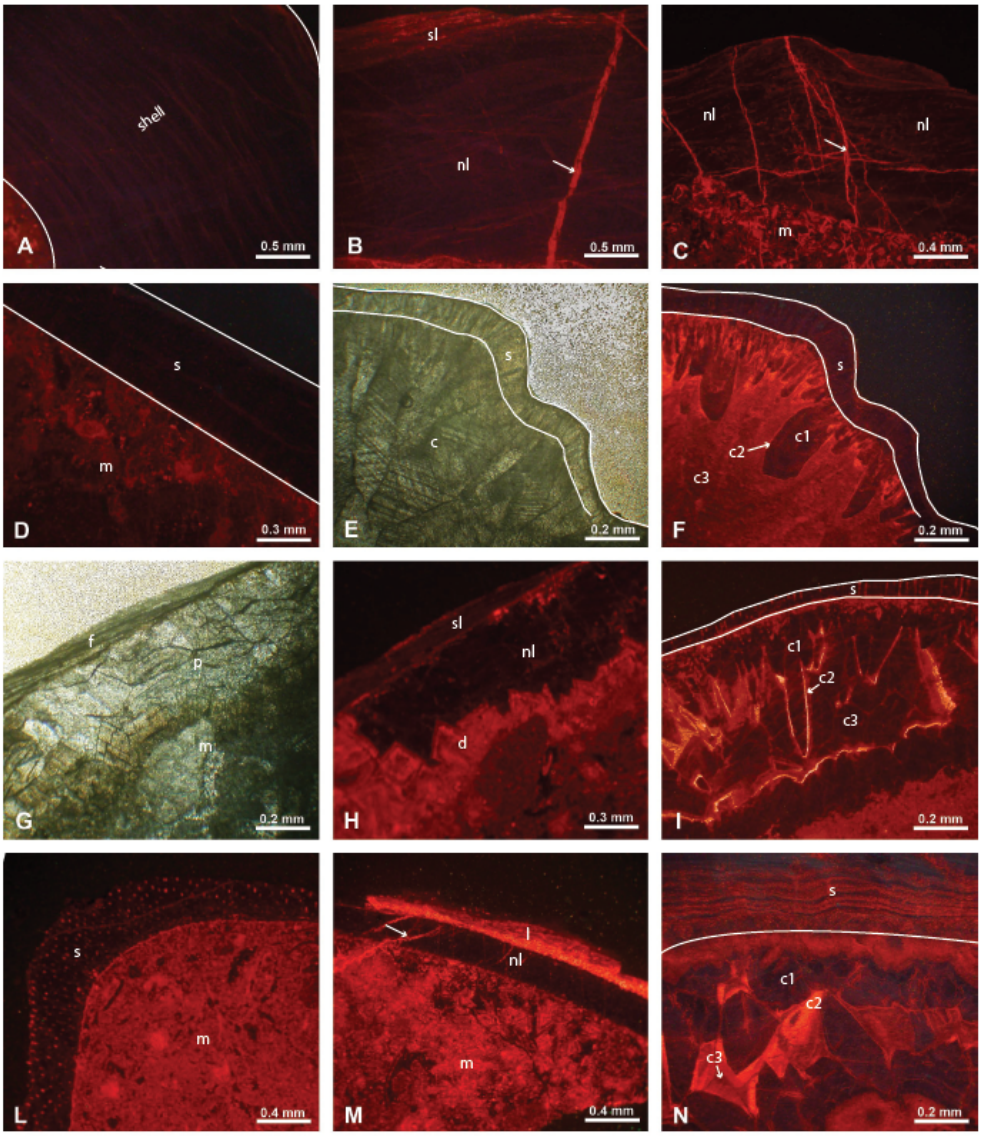
shell
A
0.5 mm
sl
nl
B
0.5 mm
nl
nl
m
C
0.4 mm
s
m
D
0.3 mm
s
c
E
0.2 mm
s
c2
c1
c3
F
0.2 mm
f
p
m
G
0.2 mm
sl
nl
d
H
0.3 mm
s
c1
c2
c3
I
0.2 mm
s
m
L
0.4 mm
l
nl
m
M
0.4 mm
s
c1
c2
c3
N
0.2 mm

Figure 4

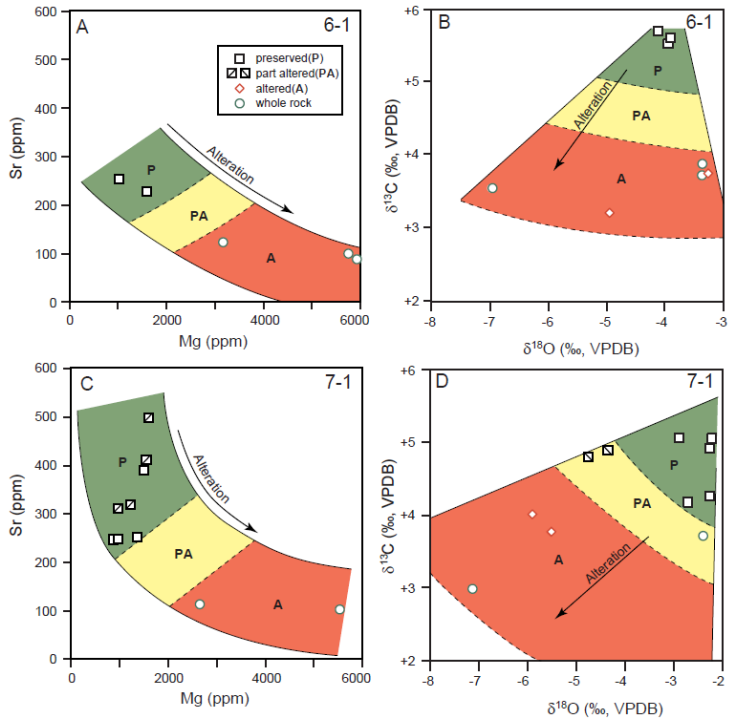

Figure 5

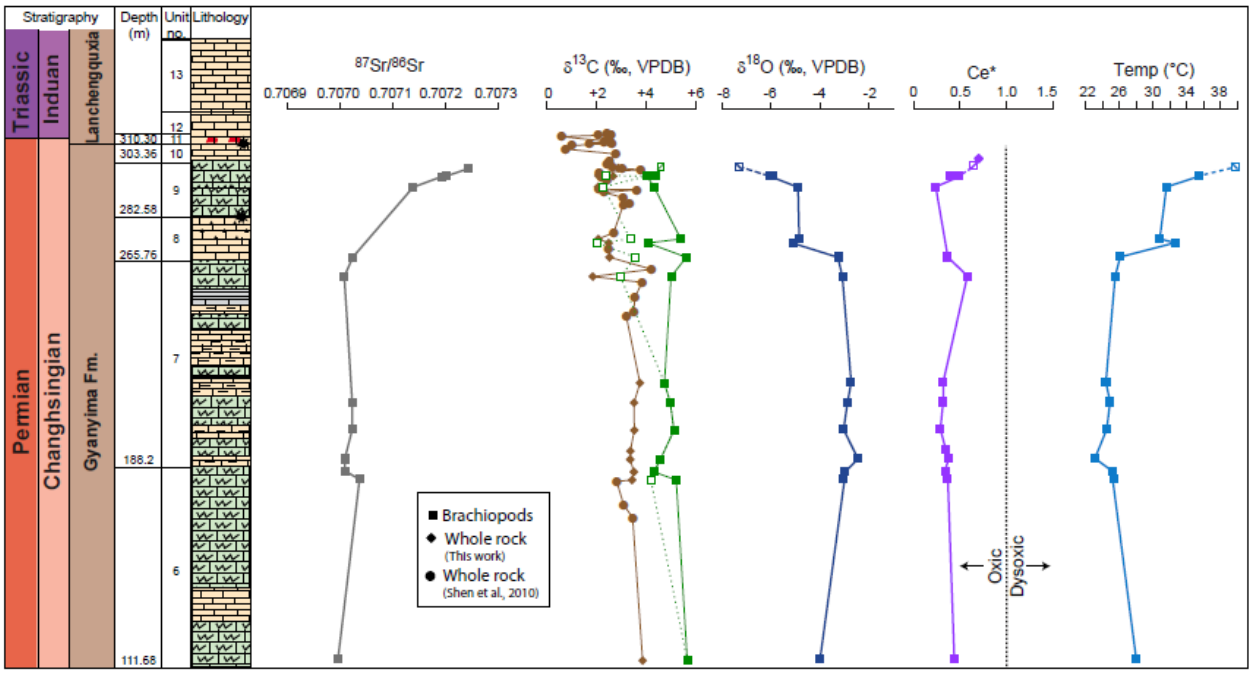

Figure 6

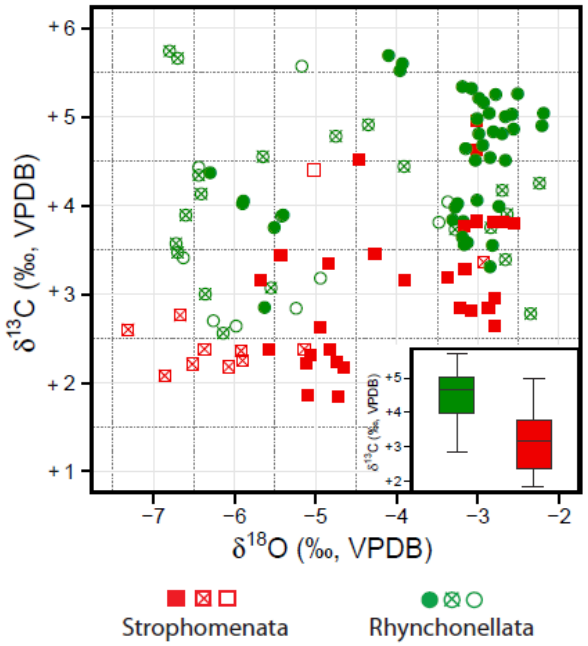

Figure 7

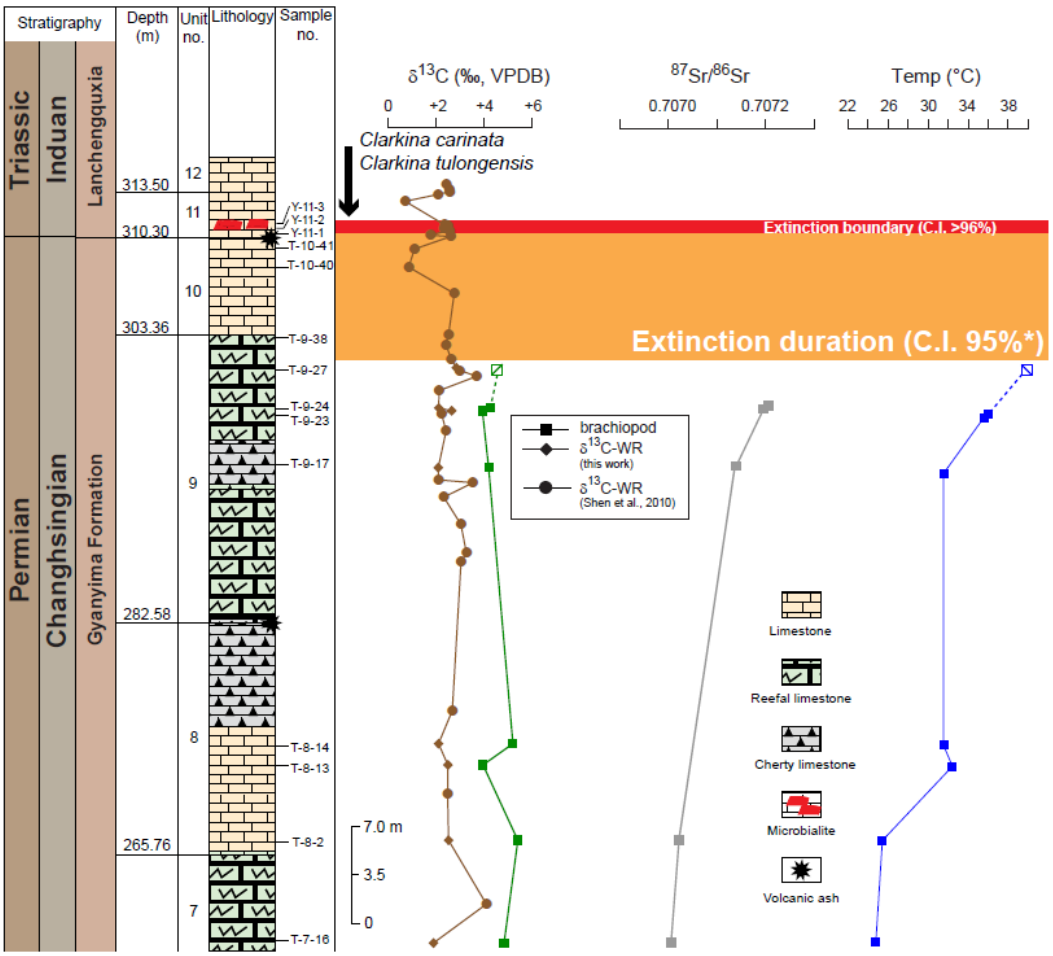

Figure 8

Table 1
Type of fabric preservation observed at SEM.

RP	Recrystallized primary layer, with calcite crystals oriented approximately perpendicular to the outer surface of the shell.
WL	Well preserved laminar secondary layer; the fabric is uniform and homogeneous, with regularly arranged interstitial spaces between structural units (blades/laths) (Fig. 3A); blades/laths have approximately the same size and show lateral continuity.
AL	Altered laminar secondary layer with heterogeneous fabric; blades/laths and interstitial spaces are randomly distributed; single blades lack lateral continuity and are irregular in shape and size; there are frequent fractures filled by diagenetic calcite.
WF	Well preserved fibrous secondary layer, showing fibers with a well-defined keel and saddle outline in cross section.
CF	Secondary layer with coarse angular profile of fibers in cross-section; this is considered an intermediate level of alteration.
AF	Altered fibrous secondary layer; fibers are amalgamated and their outline is no longer recognizable.
P	Prismatic tertiary layer with well-defined prisms with prominent growth lines, occasional calcite twinning.

1047
1048 Table 1
1049

Horizon	Sample #	Material	ΣREE	Ce/Ce*	Interpretation
6-1	PTT-4 m	Whole rock	21.201	0.421	Oxic
	PTT-55-1	Brachiopod (?)	24.798	0.532	Oxic
6-12	PTT-52 m	Whole rock	12.549	0.422	Oxic
	PTT-52-3	Brachiopod	9.103	0.310	Oxic
7-5	PTT-11 m	Whole rock	22.152	0.308	Oxic
	PTT-11-3	Brachiopod	11.835	0.311	Oxic
7-16	PTT-16-25	Brachiopod	13.487	0.578	Oxic
8-2	PTT-16 m	Whole rock	17.139	0.360	Oxic
	PTT-14 m	Whole rock	40.219	0.413	Oxic
	PTT-14-3	Brachiopod	2.242	0.354	Oxic
9-17	PTT-28 m	Whole rock	92.778	0.238	Oxic
9-23	PTT-38 m	Whole rock	22.785	0.588	Oxic
9-24	PTT-22 m	Whole rock	36.651	0.538	Oxic
	PTT-23 m	Whole rock	54.921	0.291	Oxic
Whole rock	N = 9	Mean: 0.398	SD: 0.11	p = 0.775	
Brachiopods	N = 5	Mean: 0.417	SD: 0.13		

1050
1051
1052
1053 Table 2
1054
1055
1056

Horizon	Seawater ‰ carbonate	+0.7 (B)	0.0	−0.5	+0.7 (K)	0.0	−0.5
6–1	−3.99 (3)	32.7	30.3	28.6	37.0	33.4	30.8
6–12	−2.99 (14)	29.4	27.0	25.3	31.8	28.2	25.7
6–15	−2.95 (15)	29.3	26.8	25.1	31.6	28.0	25.5
7–1	−2.44 (5)	27.3	24.9	23.2	29.0	25.5	23.0
7–3	−2.78 (5)	28.6	26.2	24.5	30.7	27.2	24.7
7–4	−2.93 (5)	29.1	26.7	25.0	31.5	27.9	25.4
7–5	−2.72 (3)	28.6	26.2	24.4	30.4	26.9	24.4
7–16	−3.08 (5)	29.7	27.3	25.5	32.3	28.7	26.2
8–2	−3.26 (3)	30.2	27.8	26.1	**33.2**	29.6	27.1
8–13	−5.11 (2)	36.7	**34.3**	32.6	43.1	39.3	36.6
8–14	−4.85 (3)	**35.9**	**33.5**	31.8	41.7	37.9	**35.2**
9–17	−4.87 (7)	**35.9**	**33.5**	31.8	41.8	38.0	**35.3**
9–23	−6.01 (6)	39.9	37.4	**35.7**	48.1	44.2	41.5
9–24	−6.05 (3)	40.0	37.5	**35.8**	48.4	44.4	41.7
9–27	−7.31 (1, altered)	44.3	41.9	40.1	55.6	51.6	48.7

Note: temperature regimes: red-unsuitable; bold — pushing the thermal adaptive limit (threshold) for brachiopods.

Table 3